PHYSICAL REVIEW E **75**, 061308 (2007)

Acoustic response of cemented granular sedimentary rocks: Molecular dynamics modeling

Xavier García[1,2] and Ernesto Medina[2,3]
[1]*Departamento de Física, Universidad Simón Bolívar, Apartado 89000, Caracas, 1080A Venezuela*
[2]*Centro de Física, Instituto Venezolano de Investigaciones Científicas. IVIC, Apartado 21827, Caracas 1020 A, Venezuela*
[3]*Department of Physics, Boston University, Boston, Massachusetts 02215, USA*

(Received 11 September 2006; published 29 June 2007)

The effect of cementation processes on the acoustical properties of sands is studied via molecular dynamics simulation methods. We propose numerical methods where the initial uncemented sand is built by simulating the settling process of sediments. Uncemented samples of different porosity are considered by emulating natural mechanical compaction of sediments due to overburden. Cementation is considered through a particle-based model that captures the underlying physics behind the process. In our simulations, we consider samples with different degrees of compaction and cementing materials with distinct elastic properties. The microstructure of cemented sands is taken into account while adding cement at specific locations within the pores, such as grain-to-grain contacts. Results show that the acoustical properties of cemented sands are strongly dependent on the amount of cement, its stiffness relative to the hosting medium, and its location within the pores. Simulation results are in good correspondence with available experimental data and compare favorably with some theoretical predictions for the sound velocity within a range of cement saturation, porosity, and confining pressure.

DOI: 10.1103/PhysRevE.75.061308 PACS number(s): 45.70.−n, 91.55.Ax, 91.60.Lj, 91.60.−x

I. INTRODUCTION

After settling, mechanical and permeating properties of sands are modified by the process of diagenesis. Among the diagenetic processes, cementation is defined in a broad sense [1] as the introduction of mineral phases into rock pores. Many mechanisms of cementation are discussed in the literature: minerals can be transported in suspension with underground waters and settle in the pores of a final hosting medium. In low-flux zones, cements can form as a solid precipitate on grain surfaces. Formation of clay bonds between grains and grain interlocking as a product of the matrix dissolution [2] are among others, possible cementation mechanisms.

Depending on their origin and location within the pores, cements modify hosting rock properties in different ways. It has been experimentally observed that, if cement is deposited near grain-to-grain contacts, it can significantly increase the strength and stiffness of granular materials [3]. In this case, grain rotation and displacement are inhibited due to cement bonds and samples develop a frame that resists compaction. In an experimental study with glass beads [4], the presence of epoxy cement at contacts was observed to prevent bead crushing during compaction. Theoretically, this effect is attributed to a more uniform stress distribution within contact areas due to cementation. This kind of cement is the main factor in rock cohesion. Therefore, the lack of this kind of cement is a potential handicap for the stability of boreholes.

A recent experimental study has addressed how cements can modify hosting rock microstructure and related hydraulic properties, such as permeability [5]. According to the authors, microstructure can be characterized through the geometric index (known as Flow zone indicator) FZI $=1/\sqrt{P_s}\tau S_v$, where P_s is a pore-shape-related value, τ is the tortuosity [6], and S_v is the specific surface area per unit of grain volume. Such a geometric index is then correlated with permeability and wave velocity. As an example, if cement is deposited uniformly on grain surfaces, a specific surface area sharply increases. On the other hand, pore-filling materials can also grow from grain surfaces towards pores, forming intertwined structures that increase tortuosity [7]. Both mechanisms lead to different microstructures at the pore scale that affect rock hydraulic and mechanical properties.

Despite the importance of the prediction of cement effects, this is often a difficult task since the exact location of cement in pores is usually unknown. Although some insight can be obtained from microphotography or other high-resolution methods, the use of these techniques is limited when considering rocks at larger (formation) scales. As an alternative, acoustical methods are of great value in the characterization of the underground to a larger extent, being successfully used in the identification of underground structures [8]. However, for a precise interpretation of acoustical logs, it is necessary to advance the understanding of the acoustics of porous media and identify the connections between macroscopic acoustic observables and microscopical petrophysical parameters. In this sense, due to the apparent linkage of rock stiffness and cementation, it seems plausible to use acoustic methods to estimate the type and amount of cement present in rocks. For this purpose, one must establish the relation between the acoustical observables, such as velocity and attenuation, cement saturation, its elastic properties, and localization within pores among other parameters.

Experimentally, the acoustical effects of coating cement were studied when considering artificially fabricated samples cemented with sodium silicate [9]. The samples showed increasing wave velocities and attenuation with cement saturation. The acoustical effects of cement located near contacts were studied experimentally by considering epoxy cement and glass beads [4]. In this work, wave velocities sharply increased with cement saturation. Similar results were reported in work by Dvorkin *et al.* [10,11] (see also references therein).

From a theoretical point of view, Dvorkin *et al.* [11] proposed a model for cemented sands based on the effective medium approach. This model considers the elastic properties of a granular material whose porosity decreases by the addition of cementing material near grain contacts. The model is based on an analytical solution of the related elasticity problem. Theoretically, it is expected that small amounts of cement added precisely at grain contacts will sharply increase rock stiffness. Different cementation schemes, where cement is added preferentially far from contacts or as a coating on grain surfaces, were considered in Ref. [12] and the results summarized by Mavko *et al.* [13]. For reference, the main formulas are also presented here in Appendix A. This theoretical formulation was proposed as an explanation for some high-velocity high-porosity samples and different velocity-porosity trends observed in North Sea sandstones [12].

Numerical methods, such as molecular dynamics or finite element methods, represent a new approach to the study of complex multibody systems such as sand. Within this approach, few numerical studies consider the effects of cementation on the mechanical and hydraulic properties of sands. In early papers, porous media were modeled using disks bonded by elastic springs representing cement [14]. The mechanical properties of this model were observed to depend on the bonding distribution and properties. A three-dimensional approach studied the brittle failure of cemented rocks under external load, modeling cement as breakable grain bonds [14].

Previous numerical studies considered cementation effects on permeability by emulating the microstructure of cemented rocks and then solving flux equations in this geometry. Some approaches consider sand as a pack of spherical particles whose radii are extracted from a given distribution. The cementation process is then simulated by increasing the grain radii by a given amount, modeling the quartz cement overgrowth [1,15]. More recent studies account for the preferential growth of cement to pores or throats by a more elaborate algorithm that simulates cement overgrowth from grain boundaries to the surface of their Voronoi polyhedra [16]. The resulting spatial correlations and other geometric characterizations were studied numerically by Biswal *et al.* [17].

However, to the best of our knowledge, the acoustics of sands, starting at the grain and cement scale, is an open problem where numerical methods can be very useful (i) to understand the underlying physics behind the phenomena, (ii) to test theoretical models, and (iii) to improve predictive capabilities. In our approach, we move a step further in the modeling of the acoustical response of cemented sands. We propose a simple particle-based method that considers the amount of cement and its location within pores.

Particle-based methods or discrete methods differ from other well-known techniques such as finite elements in that no continuous wave equations are solved directly. Instead, molecular dynamics mimics the underlying physics of wave propagation at the microscale or mesoscale using micromechanical interaction rules between discrete particles. This method involves solving Newton's equations of motion for an N-particle system and global behavior is obtained by the cooperative effect of interacting particles [18]. In our simulations we study the acoustical effects of soft and hard cements on a model sample. We consider the case when cementing material is added preferentially to grain-to-grain contacts, on grain surfaces, or as a solid material added preferentially to pore bodies. Our model sample mimics a well-sorted naturally occurring sand, capturing the underlying physics governing the acoustic pulse propagation on cemented sands.

This paper is organized in three main parts: Section II summarizes the basic concepts related to the cementation process. Section III covers a detailed description of the methods used in the simulations. Finally, simulation results are presented and discussed in Sec. IV. Important information regarding the calibration of simulations and some theoretical formulas are presented in the Appendixes.

II. CEMENTATION PROCESS

Clastic rocks are often cemented by addition of clay particles. These cements can be classified in two broad categories: detritical and diagenetical [7]. The former are transported in suspension with subsurface waters to a final location in a hosting medium where they deposit. These kinds of cementing particles are mainly attracted to the sharpest zones of pore space, such as grain-grain contacts, where the surface forces are largest [19]. These cements reinforce grain contacts and increase the rock's stiffness and sound propagation velocity. Theoretically, it is expected that even small amounts of soft cement added precisely at contacts will sharply increase the wave velocity propagation [10].

On the other hand, diagenetic cements form as precipitates of solid material initially in solution in meteoric waters (or low-mobility waters). Due to its chemical origin, many varieties of these clays are possible, depending on the concentration of different species in pore fluids and chemical equilibrium at underground pressure and temperature [7]. In this category, the so-called pore-lining clays deposit preferentially as coatings on grain surfaces, except at the grain-to-grain contacts [14]. The most frequently occurring pore-lining cements are smectite, illite, and chlorite [7,20]. These kinds of cements, if deposited homogeneously on grain surfaces, lead to a sharp increase in the specific surface area of pores while porosity reduces. Underground sections with this kind of cementation can exhibit a decrease in permeability under the normal compaction trend [5].

Another possibility for clays is to grow as long crystals from grain surfaces to pores. These kinds of clays, such as radial illite and smectite, are sometimes called pore bridging [14]. The effect of these cements is mainly to reduce porosity and permeability while increasing tortuosity. As cement is mainly deposited away from contacts, it does not significantly contribute to the sample stiffness until porosity is sufficiently reduced. Other cementing materials, such as quartz or calcite, are also present in rocks as cements. These cements can locate preferentially at pore bodies (pore-filling cements), forming tight structures. Quartz overgrowth is the formation of quartz crystals on the sand grain surface. Although crystals exhibit euhedral faces (well-formed crystal

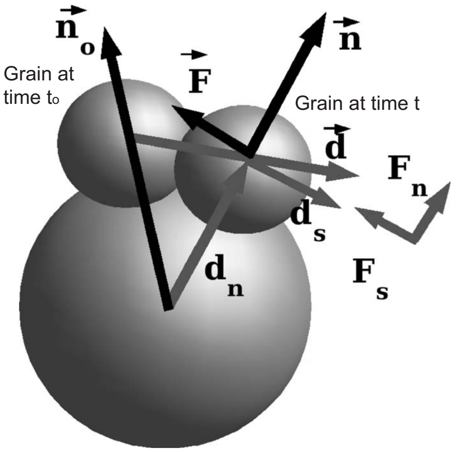

FIG. 1. Schematic representation of contact forces. Interaction forces are decomposed in normal and tangential directions to the contact area as described in the text.

faces), the overgrowth approximates also to concentric rims or coatings.

III. MODEL

A. Settling process

The initial grain pack is built by following a ballistic algorithm to simulate the settling process of clastic sands [15,21]. The procedure models sand grains as spherical particles that fall on an initially flat surface from a fixed height in the $\hat{z}$ direction and random coordinates in the xy plane. The radius of each particle is extracted from a given grain size distribution. In our simulations, the radius R of each particle is selected with equal probability in the range 0.018–0.02 cm, modeling a well-sorted sand.

During settling, Newton's equations of motion are solved for grains falling under the influence of a gravitational field $-g\hat{z}$, a viscous drag due to the aqueous medium, and interaction with other previously settled grains. At this stage, when two grains come into contact, they interact with a repulsive nonlinear viscoelastic force $\mathbf{F}_c$ given by

$$\mathbf{F}_c = \{(\kappa_n \xi - \gamma_n \dot{\xi}\}\hat{\mathbf{n}} + \mathbf{F}_s. \tag{3.1}$$

The first term in Eq. (3.1) represents the force $\mathbf{F}_n$ normal to the contact area. For the grains labeled 1 and 2 with radii R_1 and R_2 and positions $\mathbf{r}_1$ and $\mathbf{r}_2$, $\xi = \max(0, R_1 + R_2 - |\mathbf{r}_2 - \mathbf{r}_1|)$ and $\hat{\mathbf{n}}_{12} = (\mathbf{r}_1 - \mathbf{r}_2)/|\mathbf{r}_1 - \mathbf{r}_2|$ is the unitary vector joining the grains centers (see Fig. 1). The normal stiffness of the contact, $\kappa_n = 4/3\sqrt{\xi R_f}E_f$, is computed according to Hertz theory, where $R_f = (R_1 R_2)/(R_1 + R_2)$ is an effective radius and $a_c = \sqrt{\xi R_f}$ is the radius of the contact area. The effective Young's modulus E_f is calculated as $1/E_f = (1-\nu_1^2)/E_1 + (1-\nu_2^2)/E_2$, E_1, E_2, ν_1, and ν_2 being the Young modulus and Poisson's coefficient of the grain material [22]. The second term in braces in Eq. (3.1) represents the viscous forces for normal deformations, where $\gamma_n = \tilde{\gamma}_n(\xi R_f)^{1/2}$ and $\tilde{\gamma}_n$ is a damping constant:

$$\mathbf{F}_s = -\min(|\kappa_s \zeta|, \mu |F_n|)\operatorname{sgn}(\zeta)\hat{\mathbf{s}}. \tag{3.2}$$

The shear force $\mathbf{F}_s$ in Eq. (3.1) depends on the contact history and cannot be entirely determined by the position of the grains. Such force is given by Eq. (3.2), where the tangential stiffness is $\kappa_s = 8a_c G/(2-\nu)$, where the shear modulus of the grains is given by G, and ν is Poisson's coefficient. The term a_c denotes the radius of the contact area, previously defined, and μ represents the Coulomb friction coefficient. The term ζ denotes the component of the relative displacement vector in the tangential direction that took place since the time t_0, when the contact was established (see Fig. 1):

$$\zeta(t) = \int_{t_0}^{t} v_s(t')dt', \tag{3.3}$$

where $v_s = \mathbf{v}_{ij}\cdot\hat{\mathbf{s}}$ and $\hat{\mathbf{s}} = \vec{\zeta}/|\vec{\zeta}|$. The vector $\vec{\zeta}$ can be computed from the displacement vector $\mathbf{d}$ between the grains $\vec{\zeta} = \mathbf{d} - (\mathbf{d}\cdot\mathbf{n}_0)\mathbf{n}_0$ (see Fig. 1). At this stage, periodic boundary conditions are imposed on the perpendicular directions to emulate an effectively larger system and the underground natural confinement of rocks in those directions.

The initial pack models a high porosity $\phi = 41.2\%$ sand, where contacts involve marginal contact areas. The size of the generated sample was $8 \times 8 \times 32$ in units of the maximum grain diameter. Following previous results [21], this volume is several times larger than the minimum homogenization volume for the porosity of a sample with the given grain size distribution. This homogenization volume is consistent with that reported in Ref. [23] for a granular medium, like the one considered here, where it lies between 2 and 3 times the typical particle diameter. Samples with different packing are obtained by simulating the naturally occurring compaction of sediments. Following García *et al.* [21], this process is simulated by displacing, towards the center of the sample core, grains contained in frozen slabs at both ends of the sample in the $\hat{z}$ direction. Once such a macroscopic strain is imposed, ample time is allowed for grains to rearrange and relax accumulated stress. The relaxation process during compaction of granular assemblies has been recently studied in detail in Ref. [24], where both fast and slow relaxation dynamics are found. Although we carefully checked that our results did not depend on looking at longer relaxation times, logarithmic slowness offers no time scale to cut relaxation.

B. Cementation model

Once the initial sand pack is obtained, the cementation process is simulated in several steps representing different stages in the sand diagenetic history. At each step, a volume of cement is added at specific locations within the pores. Cement is added in three different ways that model cement with distinct origins and their microgeometric implications.

The procedure followed to add cement starts by discretizing the three-dimensional sample into cubic boxes of side length $c_w \approx R/10$, R being the average radius of the matrix grains. The set of cells intersects the sample voids and solid matrix, but just those cells whose center coincides with pore space are potential locations for cement. The size of these cells is obviously a drawback of the particle-based cement model due to the limited possibility of placing cement particles closer to the most angular regions of the void space—i.e., the grain contacts. This may be an important issue since the filling of such angular spaces modifies the Hertzian nature of the contacts. Such a modification has been studied analytically in Ref. [11]. Our approach, nevertheless, reproduces well the main conclusions of the previous reference: namely, even a small amount of cement increases the contact area between grains and stiffens dramatically the two grain system even for relatively soft cement.

Cells are subdivided into three groups.

(i) *Contact cells* are those that intersect two or more grains. These are located near grain contacts at the sharpest zones of pore space.

(ii) *Surface cells* are those centered in pore space and making contact with at least a single grain. Contact cells are a subset of surface cells.

(iii) *Body cells* are those centered in the pores without intersecting any grain.

The cement is added by marking, as cement saturated, a fraction of the pore-centered cells. This mark is implemented by filling with a cement particle the corresponding cell. Each cement particle represents a cubic subvolume in the sample where cement is allocated.

C. Contact cement

To model the microgeometry associated with the contact cement model, we propose an algorithm of several steps that represent a different stage in the diagenetic history of the sample. Each step involves porosity reduction due to the addition of cement to the pores. First, a small fraction of *contact cells* are marked as the cement saturated. During the following steps, an increasing number of *contact cells* are filled with cement until no *contact cells* are left. In practice, a cell is marked as cement saturated by adding a single cement particle to the center of the cell. As this particle represents a cubic subvolume c_w^3 of cement within the sample, we assign to it a mass $m_c = \rho_c c_w^3$, where ρ_c is the volumetric density of the cementing material.

After all *contact cells* are filled, further cementation steps involve the addition of cement to selected cells, neighboring those previously filled. First, we list all empty neighboring cells of those already filled with cement. Then, among these empty cells we select at random those lying closer to the grain matrix and fill them with a new cement particle. Thus, when all *contact cells* are filled, this procedure promotes cement accumulation from contacts to *surface cells*. A sequence of steps where cement was added according to the above procedure is shown in Fig. 2. The figure shows a two-dimensional example for illustrative purposes. However, results reported here refer to three-dimensional samples and smaller cells (cell width $c_w \approx 1/10$ of average grain radius).

D. Coating cement

To model the microstructure related to *coating cement*, we mark each cell with an index proportional to its distance to the solid surface. At each cementation step, all empty cells are checked and those with the smallest index (closest to matrix surface) are filled with a cement particle. In the first steps, cementing material is added on grain surfaces. As is shown in Fig. 3, further cementation steps add cement deeper into the pore bodies so that rims appear around grain surfaces. The successive cementation steps simulate several stages of the cementation history of the sample, where a change in the chemical equilibrium conditions causes precipitates to deposit uniformly on the grain surface.

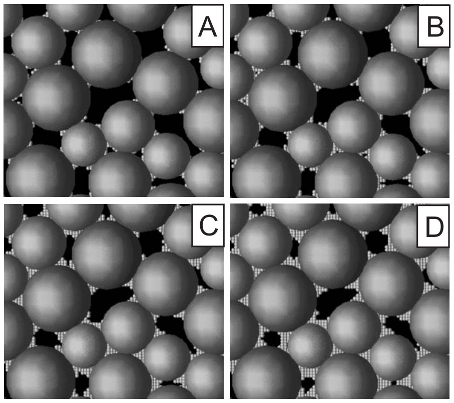

FIG. 2. Contact cement deposition. Steps *A*,*B*: an increasing number of *contact cells* is filled with cement until no contact cells are left. Then, cement grows from contacts to surfaces in steps *C* to *D*. In the figure, two-dimensional samples are shown for illustrative purposes. Reported results here refer to the three-dimensional samples.

E. Pore body cement

Simulation of *pore body cements* begins with the addition of cement particles to a fraction of surface cells selected at random. In the following steps, we check the empty cells contacting those already filled with cement. Each empty cell is then filled with a cement particle according to a probability p, proportional to the cell distance to the grain surface. This procedure simulates a preferential growth of cement from grain surfaces to pore bodies.

As shown in Fig. 4, the initial cemented cells behave as seeds for clusters that grow from the grain surface to pore bodies. The described procedure guarantees the continuity of the cement phase and simulates cementing materials in the form of long crystals attached to grain surfaces.

Cell width defines the resolution limit of the simulations. If cells are too wide, poor resolution is obtained and porosity decreases sharply to zero after a few cementation steps.

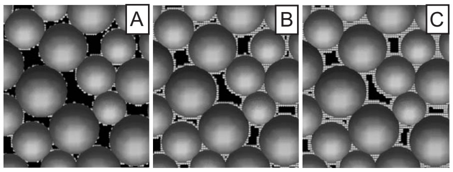

FIG. 3. Sequence of steps for *coating cement*. From step *A* to *C* cement is added to grain surfaces as a coating. This procedure simulates the homogeneous precipitation of solid material on the surface of pores. The figure shows a two-dimensional case for illustrative purposes. Reported results are for three dimensions.

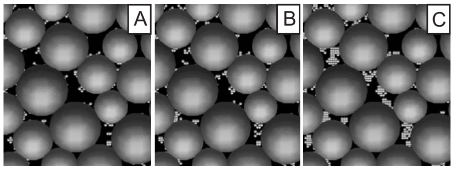

FIG. 4. Sequence of steps for *pore body cement* (also known as friable cement). Step A: initial seed of cement. Steps B,C: further cementation steps when cement is added preferentially at pore bodies. The figure shows a two-dimensional case for illustrative purposes. Reported results refer to three-dimensional samples. Note the regular structure of the cementing particles revealing the underlying lattice used to systematically position such particles.

Small cells allow more control of the final porosity of the sample at the expense of an increase in computational cost. More details about the effect of resolution on the computational cost are found in Appendix B.

F. Grain interactions

After a given porosity is reached due to cementation, we simulate acoustical pulse transmission through the sample using molecular dynamics techniques. As molecular dynamics involves the explicit solution of Newton's equations of motion for a particle-based system, we need to consider the interaction forces between the particles of the different constituents of the aggregate. In our model, particles make up the quartz matrix and cement. We do not consider fluid particles that may be in the pore volume. This approximation is justified if we suppose the fluid-saturating pores to be air, which is free to drain while the sample strains. The effect of a more incompressible saturating fluid such as water or oil could be included, and it is proposed for future work. In this way, our simulation techniques allow us to isolate the acoustical effect of cement from other agents that modify the acoustics of a real sample. With this approximation, we need only consider three kinds of interaction forces between particles: grain-to-grain forces, interaction between cement particles, and interaction forces between cement particles and grains.

In our model, the addition of cementing material is assumed not to disrupt the internal stress state of the sample. This assumption is reasonable since cementation accommodates to whatever surfaces are exposed for a given strain state. Additional strain on a cemented region can induce cement dissolution by pressure, while strain relief will induce the formation of cement. It is also a relatively slow process when compared to compaction [3]. Therefore, cement is added to pores at mechanically stable locations after grain-to-grain contacts are formed.

When a perturbation of this equilibrium state occurs, changes in the internal stress field of the sample are produced. At the pore scale, grains change their relative positions and interparticle forces change by an amount $\Delta\mathbf{F}_c$ with respect to the initial equilibrium network. If after a perturbation a pair of contacting grains labeled 1 and 2 at positions $\mathbf{r}_1$ and $\mathbf{r}_2$ are displaced to $\mathbf{r}_1+\mathbf{dr}_1$ and $\mathbf{r}_2+\mathbf{dr}_2$, respectively, their relative displacement is calculated as $\mathbf{d}=\mathbf{dr}_2-\mathbf{dr}_1$. The component of the displacement along the normal direction of the contact is given by $\Delta\xi=\mathbf{d}\cdot\hat{\mathbf{n}}$, $\hat{\mathbf{n}}=(\mathbf{r}_2-\mathbf{r}_1)/|\mathbf{r}_2-\mathbf{r}_1|$ being the unit vector joining the grain center at equilibrium. The tangential displacement is calculated as $\Delta\vec{\zeta}=\mathbf{d}-(\mathbf{d}\cdot\hat{\mathbf{n}})\hat{\mathbf{n}}$. This vector defines the tangential direction $\hat{\mathbf{s}}=\Delta\vec{\zeta}/|\Delta\vec{\zeta}|$.

TABLE I. Actual values chosen for the density, shear modulus, Poisson coefficient, and the friction coefficient (during the settling stage), in order to emulate quartz grains.

Parameter	Symbol	Value
Density $(\mathrm{kg/m^3})$	ρ_g	2.65×10^3
Shear modulus (GPa)	G	44
Poisson coefficient	ν	0.08
Friction coefficient	μ	0.3

During this stage, the force change $\Delta\mathbf{F}_c$ due to the relative displacement of contacting grains is computed according to

$$\Delta\mathbf{F}_c=\{(k_n\Delta\xi-\gamma_n\Delta\dot{\xi})\}\hat{\mathbf{n}}+\Delta\mathbf{F}_s. \tag{3.4}$$

The term κ_n in Eq. (3.4) is the elastic stiffness for normal deformations, defined previously in Eq. (3.1). However, at this stage we assume a negligible change in the contact area due to the acoustic pulse. This approximation constitutes a linearization of the Hertz force, which represents the normal grain-grain elastic interaction that acts on contact. The second term in braces in Eq. (3.4) describes the viscous forces for normal deformations. In our simulations, we have adjusted this parameter to obtain a normal restitution coefficient $e_n=0.9$, in agreement with experimental results [25,26].

The term $\Delta\mathbf{F}_s$ in Eq. (3.4) represents the change in shear force. To compute this term, we assume that no sliding between grains occurs during pulse transmission. In such case, the shear force is considered viscoelastic and calculated according to

$$\Delta\mathbf{F}_s=\{k_s\Delta\zeta-\gamma_s\Delta\dot{\zeta}\}\hat{\mathbf{s}}. \tag{3.5}$$

The first term in Eq. (3.5) represents the elastic component of the shear force. As no sliding is assumed, the tangential stiffness is computed according to Hertz-Mindlin theory, $\kappa_s=4a_cG/(2-\nu)$. The term G denotes the grains' shear modulus, ν is the material Poisson's ratio, and a_c is the radius of the initial contact area previously defined. The second term in Eq. (3.5) represents the viscous forces for shear deformations. The parameter γ_s was adjusted to obtain a tangential restitution coefficient $e_s=0.9$.

The parameters to compute forces were chosen to model quartz sand grains (see Table I). To compute forces between cement particles, we follow a procedure described by O'Brien and Bean [27]. In this procedure, cement particles are considered as nodes on the cubic lattice that discretize the sample. When a cement particle displaces from its initial position on the lattice, it interacts with its 18 closest neighbors in the lattice as shown in Fig. 5. This interaction force is calculated according to

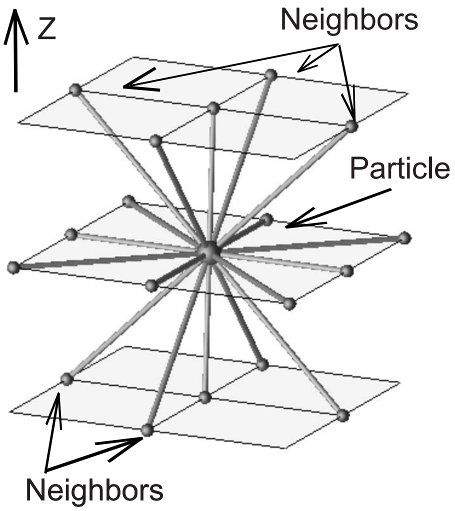

FIG. 5. Lattice representation of cement and interacting pairs of particles. Each cement particle interacts with cement particles present in each of its closest 18 nodes. The interaction force is decomposed in a component that acts along the line joining the cell center and a bending term.

$$\mathbf{f_c} = C_n[\mathbf{u}_{12} \cdot \hat{\mathbf{n}}]\hat{\mathbf{n}} + \frac{C}{|\mathbf{x}_{12}|^2}\mathbf{u}_{12}, \tag{3.6}$$

where $\mathbf{x}_{12}$ denotes the vector joining particles 1 and 2 on the undisturbed lattice and $\hat{\mathbf{n}}=\mathbf{x}_{12}/|\mathbf{x}_{12}|$. The vector $\mathbf{u}_{12}$ denotes the relative displacement of particles from their relative positions on the undisturbed lattice. The first term is the normal force with elastic constant C_n. The second term in Eq. (3.6) is the bending term, and C is an elastic constant for the interaction [27]. The force given in Eq. (3.6) can be expressed in a form similar to Eq. (3.4). However, we decided to remain as close as possible to the original reference for clarity.

Following O'Brien and Bean [27], the energy of the elastic lattice can be compared with the elastic energy of an elastic continuum. The shear elastic modulus G_c and Lamé constant λ_c of the lattice can be expressed in terms of C_n and C according to the relation

$$\lambda_c = \frac{C_n}{c_w} - \frac{2C}{c_w^3},$$

$$G_c = \frac{C_n}{c_w} + \frac{2C}{c_w^3}, \tag{3.7}$$

where c_w is the lattice parameter (in our simulations $c_w \approx 1/10$ of average grain radius):

$$V_{pc}^2 = \frac{1}{\rho_c}\left(\frac{3C_n}{c_w} + \frac{2C}{c_w^3}\right),$$

$$V_{sc}^2 = \frac{1}{\rho_c}\left(\frac{C_n}{c_w} + \frac{2C}{c_w^3}\right). \tag{3.8}$$

From linear elasticity, it is possible to express the wave velocities in the cement phase as in Eq. (3.8), where V_{pc} and V_{sc} are, respectively, the P-wave and S-wave velocities of the cementing material. The term ρ_c is the volumetric mass density of cementing material. As each cement particle represents a cubic subvolume c_w^3 of cement, such density is related to the mass of cement particles m_c:

TABLE II. Parameters used for both hard and soft cements in our simulations. The hard cement values model quartzlike cement, while the soft cement values emulate soft clays. Volumentric mass density is chosen to be the same in both cases.

Parameter	Symbol	Hard cement	Soft cement
P velocity (m/s)	V_{pc}	3.0×10^3	1.5×10^3
S velocity (m/s)	V_{sc}	1.8×10^3	9×10^2
Density (kg/m^3)	ρ_c	2.65×10^3	2.65×10^3
Poisson Coefficient	ν_c	0.22	0.22

$$C_n = \frac{1}{2}\rho_c(V_{pc}^2 - V_{sc}^2)c_w,$$

$$C = \frac{1}{4}\rho_c(3V_{pc}^2 - V_{sc}^2)c_w^3,$$

$$m_c = \rho_c c_w^3. \tag{3.9}$$

For a cement of given mass density ρ_c and wave velocities V_{pc} and V_{sc}, the mass of cement particles, m_c, and elastic constants in Eq. (3.6) are determined through Eq. (3.9). In our simulations, we considered the hard-cement and soft-cement limits compared to quartz. The parameters used in both cases are shown in Table II. The hard-cement case models a quartzlike cement such as that formed by quartz dissolution of matrix grains. The soft-cement case models a material added to pores such as soft clays. To simplify, we considered the same volumetric mass density for cement in both cases.

The third kind of interaction force arise when grains displace relative to cement particles contacting their surface. This interaction in also computed by Eq. (3.4), but the elastic constants κ_n and κ_s are now computed considering the Young's modulus and Poisson coefficient of quartz and cement. The diameter of the contact area is taken as the cement cell width c_w. In this manner, a grain feels a force due its contacting grains and due to cement particles contacting its surface.

G. Acoustics

In order to perform acoustic tests, the sample is subdivided along the propagation axis $\hat{z}$ into parallel slabs of the two largest grains diameters. A square-wave displacement is imposed on grains contained in one end slab of the sample while the other end slab is kept fixed as is shown in Fig. 6. The former boundary condition emulates the setup of an acoustic measurement. The fixed boundary condition on the opposite end prevents the sample from displacing as a whole.

The imposed strain displaces grains from their original equilibrium positions and disrupts the initial force network.

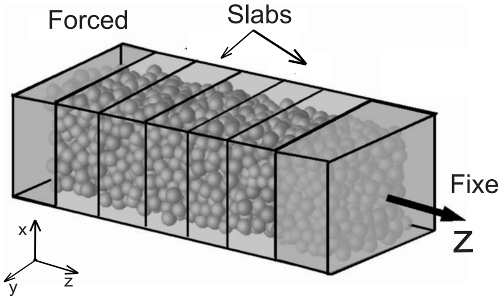

FIG. 6. Sample volume is discretized into parallel slabs along the $\hat{z}$ axis. At one end, a square-wave displacement is imposed while the opposite slab is fixed. Average forces on grains contained in each slab are calculated as a function of time to track the pulse position and amplitude. The slab at one end is forced while the opposite one is frozen.

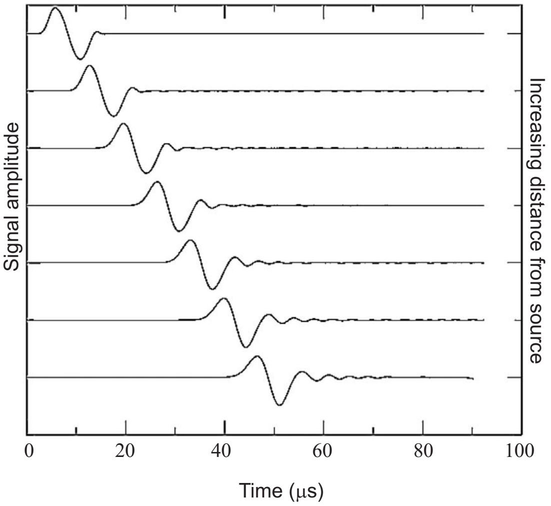

FIG. 7. Acoustical signals received at simulated detectors. Signals recorded, correspond to the average force along $\hat{z}$ of grains and cement particles in different slabs of the sample. From top to bottom, signals are recorded at detectors located increasingly farther from the source.

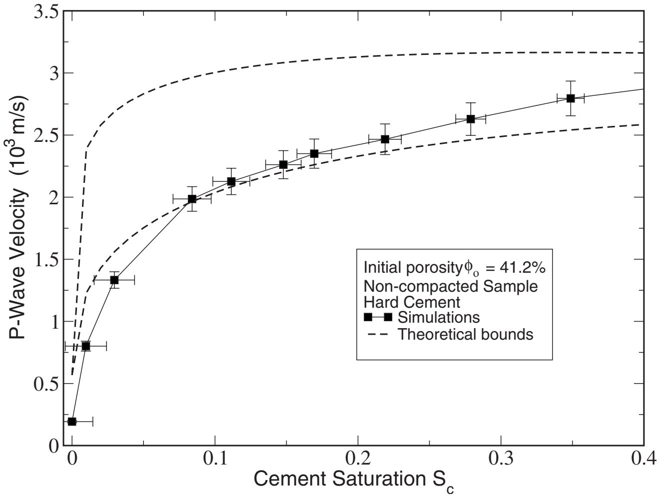

FIG. 8. *P*-wave velocity versus porosity computed for different cement saturations S_c of cement added near contacts in an initially uncompacted sample. Small amounts of contact cement contribute to increase the stiffness of the composite. As more cement is added, it locates farther from contacts and stiffness increases at a smaller rate. Consequently, the $V_p(S_c)$ trend shows a characteristic downward concavity.

This perturbation propagates in the form of an acoustic pulse with a well-defined central frequency. To keep track of the pulse position and amplitude, we monitor changes in the forces felt by grains as a function of time and position. The average of the force along z over the grains contained in each slab at time t is taken as the acoustical signal $A(z,t)$ at the position of the slab center z. This value is calculated according to the relation

$$A(z,t) = \frac{1}{N_i}\sum_{i}^{N} f_i, \tag{3.10}$$

where the term f_i is the force change at time t on the ith grain or cement particle in the slab. The summation index runs over N particles in the slab. This procedure simulates a set of acoustical detectors distributed along the sample. As Fig. 7 shows, the position in time of the stress pulse can be tracked by comparing signals received in different detectors, so that the pulse velocity V_p can be computed according to

$$V_p = \frac{L}{T_2 - T_1} \pm \frac{L\Delta T + T\Delta L}{(T_2 - T_1)^2}, \tag{3.11}$$

by comparing the arrival times T_1 and T_2 of the signal maximum in two detectors separated by a distance of L. The error in pulse position, $\Delta L \approx R$, is estimated as the half width of slabs, $\approx 2R$. The error in the time arrival ΔT is taken as the time spacing between two consecutive calculations of the force average in the slabs.

In this work we will only address P waves for two reasons: (i) We find that for the sample sizes we have used, shear and pressure waves are very strongly coupled and it is difficult to achieve a clean shear signal in order to perform reliable velocity calculations. (ii) The shear waves are strongly damped, which results in very weak signals that are difficult to assess without large error bars.

IV. RESULTS AND DISCUSSION

We simulate acoustic pulse propagation through a cemented sand. Cement is preferentially added near grain-to-grain contacts following the procedure described in Sec. III C, and its elastic properties are given in the column labeled “Hard cement” in Table II. These parameters are suited to model a quartzlike cement and commonly used cements in experiments [13,28]. This initial system mimics a well-sorted and noncompacted sand with porosity ϕ=41.2% and point grain-to-grain contacts. We refer to this system as the noncompacted sample. Porosity reduction of the initial high-porosity sample is achieved in several steps in which varying amounts of cement are added within pores. Acoustic pulse propagation is then simulated for different degrees of cement saturation S_c. As shown in Fig. 8, we observe an increase in sound velocity when a small amount of cement is added preferentially near grain contacts. This trend occurs because cement increases the restoring force of contacts and bridge grains initially separated. As a result, the stiffness of the sample increases at a higher rate than the porosity is reduced. Consequently, the V_p trend shows a downward concavity. As has been pointed before by Dvorkin and Nur [12], this is a consistent explanation of some observed high-porosity and velocity samples. When more cement is added, porosity reduces and particles tend to locate progressively farther from contacts. In this case, stiffness increases at a slower rate than in the higher-porosity range, when cement particles locate precisely at contacts. The net result is a decreasing slope of the velocity-porosity curve as porosity is reduced.

The P-wave velocities in Fig. 8 are measured under uniaxial stress conditions. Under these conditions one expects stress anisotropy and thus velocity anisotropy [29,30]. We have indeed verified such anisotropy in our model to be of 20% at 100 MPa of uniaxial stress in the absence of cementation. To compare our results with effective medium approximations we resort to the model of Dvorkin, Nur, and Yin [11,12], where although *isotropy is assumed*, it is useful to test the effects of cement localization. With this proviso in mind we plot in Fig. 8 the theoretical bounds for the sound velocity of the cemented sample. Both theoretical curves were obtained with the formulas given in Appendix A for the simulation parameters. The upper trend (high velocity) corresponds to the idealized case when all cement is precisely added at contacts. The low-velocity trend corresponds to a scheme in which cement is added uniformly on the grain surface.

As shown in Fig. 8, the obtained velocity-porosity trends for the noncompacted sample with contact cement have the same qualitative behavior as the theoretical predictions. However, the theory predicts a very sharp velocity rise when a small amount of cement is first added. Beyond the initial velocity rise, theoretical curves tend to saturate rapidly. Instead, we observe a soft continuous velocity increase with cement saturation S_c. For a set of parameters close to ours, previous experimental studies report a similar qualitative behavior for a system of beads cemented with solidified epoxy [4,11,28]. The experimental results lie between both theoretical curves [11] even though the experimental situation involves anisotropy due to uniaxial stress.

We attribute this discrepancy, of both the theory and experiments, with our results to the stiffness of the initial uncemented sample. Theoretically, a finite nonvanishing velocity is expected for the uncemented samples regardless of the effects confining pressure. For the case shown in Fig. 8, the minimal theoretical velocity is higher than that obtained in our simulations. Results in the aforementioned experiments deal with compacted samples that, uncemented, propagate sound at velocities higher than the minimum predicted by the theory [4]. On the other hand, in our settling algorithm grains settle due gravitational forces and no confining pressure is applied. As a result, we obtain very loose samples with marginal contact areas where the P-wave velocity can be quite smaller. Aiming at better reproducing common experimental setups used for rocks, we simulated the compaction of the uncemented sample to a porosity ϕ=38.6%. At this porosity, the confining pressure was recorded as $P_c \approx 30$ MPa and the sound velocity was observed to increase from V_p =0.2 to 1.7 km/s, similar to the minimal velocity reported in the aforementioned experiments [11]. Then, the cementation process was simulated as in the previous case and acoustic tests were performed for different cement saturations.

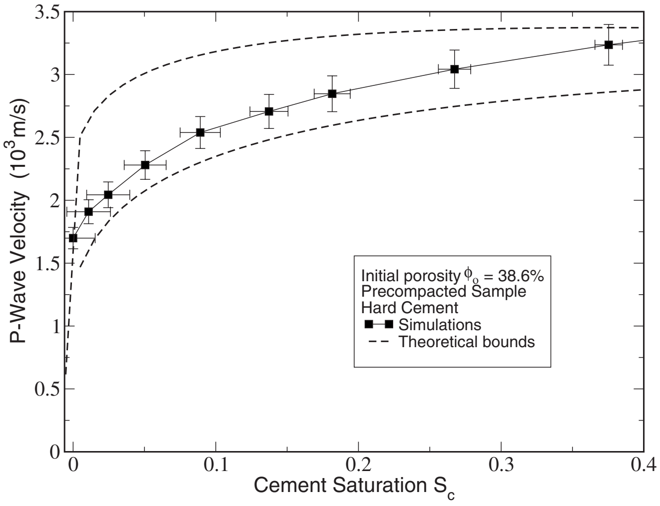

FIG. 9. P-wave velocity versus porosity computed for different cement saturations in a precompacted sample of porosity ϕ =38.4%. Uncemented sample is compacted with 30 MPa confining pressure. After compaction, cement is added preferentially near contacts. Theoretical predictions can be good estimates of velocity bounds for precompacted samples.

As expected, Fig. 9 shows that for zero cement saturation, the velocity is higher in the compacted sample than in the uncompacted sample. Furthermore, the figure shows that in the case of the compacted sample, the velocity increases at a slower rate when cement saturation S_c increases. The net result is that the velocity trend for the compacted sample lies between theoretical curves. In this case, for the range of cement saturation S_c shown in Fig. 9, the obtained results are in good quantitative agreement with available experimental data reported in previous works [11,12,28]. It should be noted that for the case of the compacted sample, theoretical curves are slightly different from those of the uncompacted sample, since coordination and porosity are different. Nevertheless, these variations are relatively small.

These results suggest that the confining pressure of the initial uncemented sample is a crucial parameter which determines the velocity trends obtained after adding small amounts of cement. This is an intuitive result since for loose sediments close to a suspension, stiffness is negligible. Then, any stiffness increase due to cementation can be several times the initial one and represents a large fraction of the final stiffness of the cemented sample.

The results in Figs. 8 and 9 suggest that contact cement theory may work well for samples which are cemented after some compaction is achieved. However, it may overestimate the sound velocity for the case of cement added to weakly compacted media—i.e., unconsolidated sands. The latter case can be that of artificially cemented granular materials such as young sediments cemented with perforation mud or laboratory-produced materials. We believe that the case

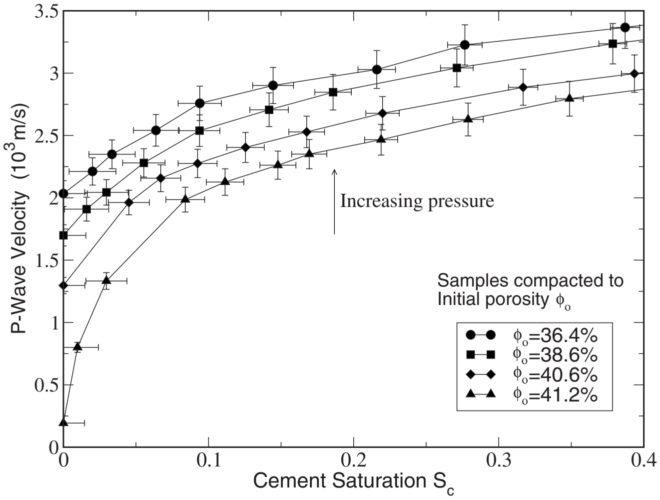

FIG. 10. *P*-wave velocity versus cement saturation in a set of samples precompacted to different initial porosity ϕ_0. Each curve represents a possible diagenetic path for a granular material. Samples are first compacted to a porosity ϕ_0 due to burial. Then, cementation processes begin. The more compacted the samples, the smaller the relative increase of velocity with S_c.

where cement is added after some compaction is the most realistic for rocks, since a chemical cementation is achieved after some pressure-temperature conditions are reached with burial. This behavior is further illustrated in Fig. 10 where results are shown for several cases in which cementation starts after some compaction. In this figure, each trend may represent a possible diagenetic path followed by a granular material. The starting framework in all cases is that of a very loose material of porosity ϕ=41.2%, representing sediments after settling. The initial loose pack is then compacted to a porosity ϕ_0, simulating the mechanical effects of burial. After compaction, a relatively hard cementing material is added in varying amounts.

As shown in Fig. 11, we observed the same qualitative behavior when considering cementing materials with different elastic properties. In the figure, the sound velocity in the uncompacted sample increases by a factor of ≈10 when a relatively hard cement saturation varies from 0 to 0.1. For the same cement saturation, a relatively soft cement increases sound velocity by a factor of ≈7. In the case of a compacted (stiffer) sample, this variation approximates to ≈25% in the case of the hard cement and ≈12% for the soft cement. According to these results, the velocity rise in soft samples mainly depends on the amount of cement while in stiff samples the most relevant factor is the type of cement.

Cement can also accumulate as a *coating cement* on grain surfaces or at pore bodies far from contacts. The former can be the case when cement precipitates as a solid material in low-flux zones [7]. The latter case is encountered in some sands which are held together by confining pressure only. Following Dvorkin and Nur [12], this kind of cement is termed here as *friable* or *pore body cement*. This geometric character of the cementation process can be explored in our simulations by following the details given in Sec. III D for *coating cement* and Sec. III E for *friable cement*. Methods to simulate the case of cement at contacts, treated previously, are discussed in Sec. III C.

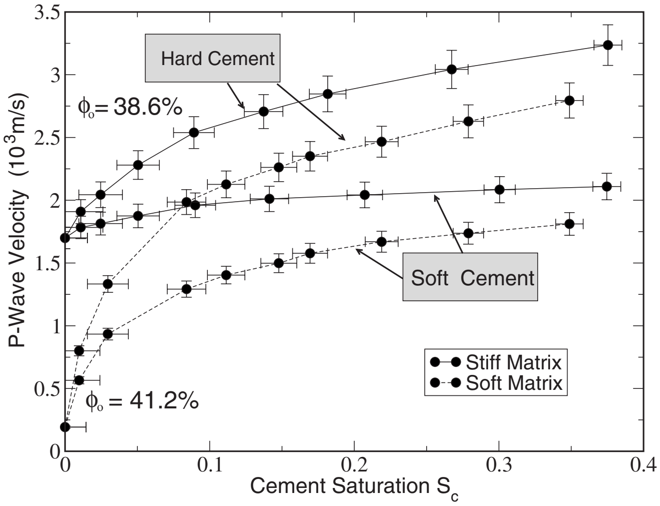

FIG. 11. *P*-wave velocity for samples with different initial compaction, cemented with two different types of cement. The velocity increase in soft samples depends mainly in the amount of cement. For stiff samples, the velocity increase depends strongly on the elastic properties of cement.

In Fig. 12, the lowest-velocity trend is obtained when solid cement is added preferentially as pore-filling material. Since this kind of cement accumulates far from contacts, it contributes marginally to rock stiffness. The main effect of this kind of cement is to reduce porosity. As more pore-filling material is added, cement particles start to bridge separated grains. Then, blocks of cement particles are also compressed during pulse propagation with the net effect of an increasing slope of velocity trend as porosity reduces. It is to be noticed that if clays were added during settling, one should expect a different behavior. In that case, above a critical concentration of clays (about ≈40%), they become load bearing and completely surround disconnected quartz grains.

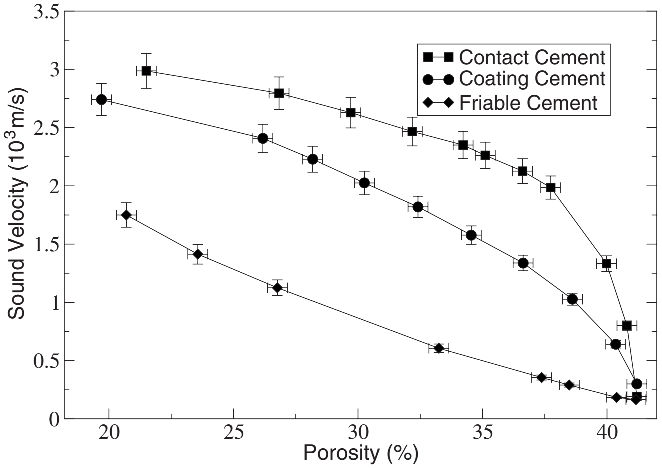

FIG. 12. Acoustic response for three different cementation schemes. The acoustical response depends on the microstructure details. Contact cement leads to a downward concavity in the $V_p(S_c)$ trend with decreasing slope as cement saturation increases. Friable cement leads to the opposite behavior. Coating cement corresponds to an intermediate case.

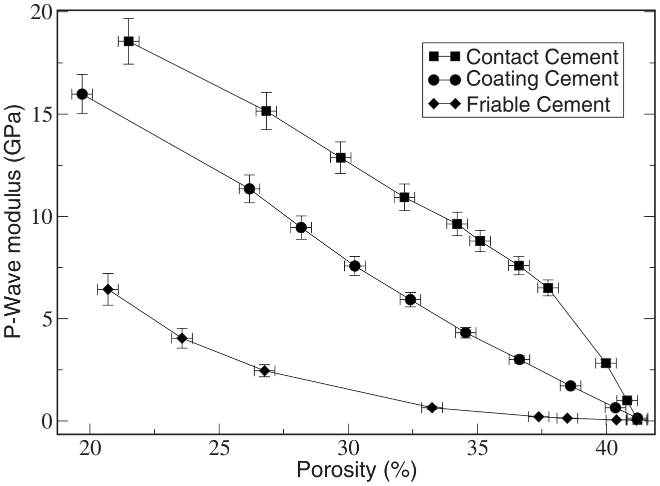

FIG. 13. *P*-wave modulus against porosity for three different cementation schemes. For medium to high cement saturation, contact cement leads to a quasilinear trend for the *P*-wave modulus with porosity in agreement with experimental results [10]. Coating cement and friable sands show an upward concavity observed in some naturally occurring sands [12].

In such a case, soft clays dominate the acoustics and the velocity decreases for porosities below some threshold value [4].

Figure 12 shows a monotonic velocity increase with cement saturation. Here, clays or any other cementing material is added after settling. Therefore, quartz grains remain in contact in the whole porosity range. As a consequence, soft clays may reduce porosity but sound velocity can only decrease slightly due to inertial effects. This result suggests that for low-porosity sands with high clay content, high sound velocity should be expected if clays are of diagenetical origin. The low porosity velocity can be related to the depositional origin of clays. This may be an important factor to consider when reconstructing the history of a reservoir sample.

The velocity trend for coating cement lies in between the limiting cases of friable and contact cement. In this case, a fraction of cement deposits near contacts and contributes to rock stiffness, while a significant volume of cement mainly reduces porosity. Figure 12 shows that for the same porosity, this kind of cementation leads to higher velocities than those of friable sand and lower velocities than those of the contact-cemented sample. These results show that microstructural details are very important parameters that influence the velocity-porosity trends of cemented samples. To further compare our results with available experimental data, we calculated the *P*-wave modulus from results in Fig. 12. The computed moduli are shown against porosity in Fig. 13. As expected, the results in Fig. 13 show different trends for the *P*-wave modulus depending on the amount of cement and the cementation scheme. In the case of contact cement, a quasilinear trend is observed for cement saturations above $\approx 10\%$. This result qualitatively coincides with previous experimental results reported in [10] and references therein. Similar behavior was observed for the case of coating cement. Nevertheless, the *P* modulus is smaller for the range of cement saturation studied. Velocity trends obtained for the case of friable cement can be compared with experimental data obtained for some samples with scarce intergranular cement [10]. These results are in good agreement with the various correlations between *P* modulus and porosity observed in reservoir sands.

It must be noted that details of the microstructure are hardly included in most theoretical approximations. Some models treat the case of a two-phase composite and/or spherical inclusions, of little use in the range $0\% < S_c < 100\%$. For instance, the Hashin-Shtrikman model establishes bounds on the maximum and minimum elastic moduli at zero porosity ($S_c = 100\%$). Although a generalization of this model would allow us to calculate bounds for the moduli at intermediate porosities [13], in our simulations and in the experiments considered, voids are filled with air with negligible elastic modulus. In this case, the lower bound for the moduli is trivial (zero) in the entire range of cement saturation considered. Although the contact cement model explicitly includes the microstructure, some of the assumptions made in the theory are not valid for large amounts of cement.

We must finally make comments on the issue of uniaxial stress-induced anisotropy. We will only comment on the case without any cement present: Stress anisotropy exists in our samples borne from the construction of the granular pack under the action of gravity. Nevertheless, in our models, *velocity anisotropy* only exists after the sample has been compacted to porosities below 40% or above 25 MPa of applied stress. Then the velocity parallel to the strain axis is greater than perpendicular to it. At 100 MPa of stress the anisotropy is 20% and it roughly saturates beyond this point up to stresses of more than 250 MPa corresponding to porosities of 37%. This scenario is very close to that of recent experiments by Vega, Mavko, and Prasad [30] and an experimental and theoretical treatment of Johnson *et al.* [29] for nonconsolidated grain packs. An additional finding of the latter work is the existence of a velocity dependence on the deformation history or hysteresis of the pack, which is demonstrated both theoretically and in experiments. This effect is also manifest in the experiments of Ref. [30]. Our model also reproduces hysteresis effects in granular packs without cement. Extensive simulations regarding this issue were reported in Ref. [31].

V. CONCLUSIONS

Simulation results show that cements modify the elastic properties of sands in a different manner, depending on the relative stiffness of cement and the hosting medium, the amount of cement, and its localization within the pores. If cement is added preferentially near contacts, it can contribute noticeably to the stiffness of the composite, the effect being enhanced in uncompacted granular samples. Friable cement leads to relatively low-velocity samples even for moderate cement saturations. Velocity trends show characteristic concavities in each case.

As the confining pressure increases, the host medium for the cement becomes stiffer by compaction and cements have a smaller effect on the sound velocity of the final composite.

As a result, velocity-porosity trends differ for samples that follow different compaction-cementation paths. Although contact cement theory does not account for the confining pressure effects or anisotropy produced by uniaxial stress, it can give a good estimate of the sound velocity in precompacted samples with small amounts of contact cement ($S_c < 15\%$).

The simulation results presented, qualitatively and quantitatively, reproduce the available experimental data where porosity is reduced and velocity is increased due to cementation. The proposed methods are suited to take into account the microstructural details of cementation processes and their acoustical implications. As these details are hardly included in most effective medium approximations, simulation techniques can be considered an alternative tool to model the acoustics of cemented sands and achieve new insights into the underlying physics behind the phenomena.

ACKNOWLEDGMENTS

This work was supported by the IVIC Rocks project and by FONACIT through Grant No. S1-2001000910.

APPENDIX A: EFFECTIVE MEDIUM APPROXIMATION FOR CEMENTED SANDS

According to the theoretical model proposed by Dvorkin *et al.* [10–12] the initial porosity ϕ_0 of an uncemented sample is decreased to ϕ by the addition of cementing material. Once a given volume of cement is added, the effective bulk K_f and shear G_f moduli of the composite are calculated according to

$$K_f = \frac{1}{6} N(1-\phi_0) M_c \hat{S}_n,$$

$$G_f = \frac{3}{5} K_f + \frac{3}{20} N(1-\phi_0) G_c \hat{S}_t,$$

$$M_c = V_{pc}^2 \rho_c,$$

$$G_c = V_{sc}^2 \rho_c, \tag{A1}$$

where ρ_c, V_{pc}, and V_{sc} are mass density, P-wave velocity, and S-wave velocity of cementing material and N is the average number of contacts per grain. The normal and tangential stiffnesses of the contacts in the cemented sample, denoted as $\hat{S}_n$ and $\hat{S}_t$, respectively, are given as function of porosity change due to cementation:

$$\hat{S}_n = A_n \alpha^2 + B_n \alpha + C_n,$$

$$\hat{S}_t = A_s \alpha^2 + B_s \alpha + C_s, \tag{A2}$$

where

$$\alpha = \begin{cases} \left(\dfrac{2}{3} \dfrac{\phi_0 - \phi}{1-\phi_0} \right)^{1/2} & \text{for cement in layers,} \\ 2\left(\dfrac{1}{3N} \dfrac{\phi_0 - \phi}{1-\phi_0} \right)^{1/4} & \text{for cement at contacts.} \end{cases} \tag{A3}$$

The coefficients of the α powers in Eq. (A2) are given by the relations

$$A_n = -0.024153 \Lambda_n^{-1.3646},$$

$$B_n = 0.20405 \Lambda_n^{-0.89008},$$

$$C_n = 0.00024649 \Lambda_n^{-1.9864}, \tag{A4}$$

$$A_s = -10^{-2}(2.26\nu^2 + 2.07\nu + 2.3)\Lambda_s^{\omega_1},$$

$$B_s = (0.0573\nu^2 + 0.0937\nu + 0.202)\Lambda_s^{\omega_2},$$

$$C_s = -10^{-4}(9.654\nu^2 + 4.945\nu + 3.1)\Lambda_s^{\omega_3}, \tag{A5}$$

where

$$\omega_1 = (0.08167\nu^2 + 0.4011\nu - 1.8186),$$

$$\omega_2 = (0.027\nu^2 + 0.0529\nu - 0.8765),$$

$$\omega_3 = (0.079\nu^2 + 0.1754\nu - 1.342),$$

$$\Lambda_n = \frac{2G_c}{\pi G} \frac{(1-\nu)(1-\nu_c)}{1-2\nu_c},$$

$$\Lambda_s = \frac{G_c}{\pi G}, \tag{A6}$$

where ν and ν_c are, respectively, the grain and cement Poisson ratios, G is the shear modulus of grains, and the rest of the symbols have the same denotation as in the previous equation.

The theoretical predictions for the P-wave velocity are then obtained for the cemented sample by substituting elastic moduli given in Eq. (A1) into the linear elasticity, Eq. (A7):

$$V_p = \left(\frac{K_f + 4G_f/3}{\rho_f} \right)^{1/2}, \tag{A7}$$

where V_p is the sound velocity of the composite system of grains and cement and ρ_f the effective mass density. In our simulations, we have used Eq. (A7) to fit the obtained data.

APPENDIX B: THE EFFECT OF RESOLUTION IN THE COMPUTATIONAL COST

The resolution Ω affects the computational cost in three different ways: first, the cell width $c_w \approx R/\Omega$, R being the average grain radii. As Ω increases, c_w reduces and the number of cells to discretize the sample increases as $\approx \Omega^3$ in three dimensions. The larger the number of cells, the larger the memory needed to store the information related to each cell. Additionally, as the number of cement particles rises, the number of operations to compute forces, velocities, and actualize positions increases proportionally.

On the other hand, for smaller cell widths c_w, the mass of cement particles goes as $m_c \approx \Omega^{-3}$ and elastic stiffness constants go as $\kappa \approx \Omega^{-1}$. The characteristic integration step t_c is determined by the characteristic time related to the interactions, $t_c \approx (m_c/\kappa)^{1/2} \approx \Omega$. Therefore, as the resolution Ω increases, the number of integration steps needed to simulate a given time interval, rises linearly. As both the number of cement particles and integration steps increase, the computational cost is higher.

---

[1] S. Bryant, C. Cade, and D. Mellor, AAPG Bull. **77**, 1338 (1993).

[2] E. Gundersen, F. Renand, D. K. Dysthe, K. Bjotlykke, and B. Jamtveit, J. Geophys. Res. **107**, 1 (2002).

[3] Y. Bernabé, D. T. Fryer, and J. A. Hayes, Geophys. Res. Lett. **19**, 1511 (1992).

[4] H. Yin, Ph.D. thesis, Stanford University, 1992.

[5] M. Prasad, Geophysics **68**, 108 (2003).

[6] R. P. Ewing and R. Horton, Water Resour. Res. **38**, 1285 (2002).

[7] N. Manmath and W. L. Lake, AAPG Bull. **79**, 431 (1995).

[8] R. M. Mitchum, J. B. Sangree, P. R. Vail, and W. W. Wornhart, AAPG Mem. **58**, 163 (1995).

[9] S. Nakagawa and L. R. Myer, http://www.osti.gov/energycitations/servlets/purl/799643-musbfh/native/.

[10] J. Dvorkin, J. Berryman, and A. Nur, Mech. Mater. **31**, 461 (1999).

[11] J. Dvorkin, A. Nur, and H. Yin, Mech. Mater. **18**, 351 (1994).

[12] J. Dvorkin and A. Nur, Geophysics **61**, 1363 (1996).

[13] G. M. Mavko, T. Mukerji, and J. Dvorkin, *The Rock Physics Handbook* (Cambridge University Press, Cambridge, England, 1988).

[14] J. Guodong, T. W. Patzek, and D. B. Silin, SPE J. **83587**, 1 (2003).

[15] S. Bakke and P. E. Oren, SPE J. **35479**, 35 (1997).

[16] L. M. Schwartz and S. Kimminau, Geophysics **52**, 1402 (1987).

[17] B. Biswal, C. Manwart, R. Hilfer, S. Bakke, and P. E. Oren, Physica A **273**, 452 (1999).

[18] D. C. Rapaport, *The Art of Molecular Dynamics Simulation* (Cambridge University Press, Cambridge, England, 1995).

[19] A. W. Adamson and A. P. Gast, *Physical Chemistry of Surfaces* (Wiley Interscience, New York, 1982).

[20] M. Sahimi, *Applications of Percolation Theory* (Taylor & Francis, London, 1994).

[21] X. García, M. Araujo, and E. Medina, Waves Random Media **14**, 129 (2004).

[22] A. Love, *A Treatise on the Mathematical Theory of Elasticity* (Dover, New York, 1944).

[23] T. Bourbie, O. Coussy, and B. Zinszner, *Acoustics of Porous Media* (Gulf, Houston, 1987).

[24] J. Brujic, P. Wang, C. Song, D. Johnson, O. Sindt, and H. Makse, Phys. Rev. Lett. **95**, 128001 (2005); H. A. Makse, N. Gland, D. L. Johnson, and L. Schwartz, Phys. Rev. E **70**, 061302 (2004).

[25] G. Kuwabara and K. Kono, Jpn. J. Appl. Phys., Part 1 **26**, 1230 (1987).

[26] J. Schafer, S. Dippel, and D. E. Wolf, J. Phys. I **6**, 5 (1996).

[27] G. S. O'Brien and J. Bean, Geophys. Res. Lett. **31**, 1 (2004).

[28] H. Yin and J. Dvorkin, Geophys. Res. Lett. **21**, 903 (1994).

[29] D. L. Johnson, L. M. Schwartz, D. Elata, J. G. Berryman, B. Hornby, and A. N. Norris, ASME J. Appl. Mech. **65**, 380 (1998).

[30] S. Vega, G. Mavko, and M. Prasad, The Leading Edge **25**, 252 (2006).

[31] X. García and E. Medina, Geophysics **71**, 13 (2006).